

RoHOI: Robustness Benchmark for Human-Object Interaction Detection

Di Wen¹ Kunyu Peng^{1,*} Kailun Yang² Yufan Chen¹ Ruiping Liu¹ Junwei Zheng¹
 Alina Roitberg³ Rainer Stiefelhagen¹
¹Karlsruhe Institute of Technology ²Hunan University ³University of Stuttgart

Abstract

Human-Object Interaction (HOI) detection is crucial for robot-human assistance, enabling context-aware support. However, models trained on clean datasets degrade in real-world conditions due to unforeseen corruptions, leading to inaccurate prediction. To address this, we introduce the first robustness benchmark for HOI detection, evaluating model resilience under diverse challenges. Despite advances, current models struggle with environmental variability, occlusion, and noise. Our benchmark, RoHOI, includes 20 corruption types based on HICO-DET and V-COCO datasets and a new robustness-focused metric. We systematically analyze existing models in the related field, revealing significant performance drops under corruptions. To improve robustness, we propose a Semantic-Aware Masking-based Progressive Learning (SAMPL) strategy to guide the model to be optimized based on holistic and partial cues, dynamically adjusting the model's optimization to enhance robust feature learning. Extensive experiments show our approach outperforms state-of-the-art methods, setting a new standard for robust HOI detection. Benchmarks, datasets, and code will be made publicly available at <https://github.com/Kratos-Wen/RoHOI>.

1. Introduction

Human-Object Interaction (HOI) detection is a key task in visual scene understanding, involving the identification and interpretation of interactions between humans and objects in an image [19, 20, 25, 26, 56, 78]. It serves as a foundation for many critical applications, including autonomous driving [45, 48], robotics [65], video surveillance [10, 50], and augmented reality [76], where a fine-grained understanding of human behavior and object interactions is paramount [13]. In recent years, transformer-based models [57, 78, 82] and Vision-Language Models (VLMs) [2, 8, 12], have achieved impressive success in HOI detection field. These models excel at capturing in-

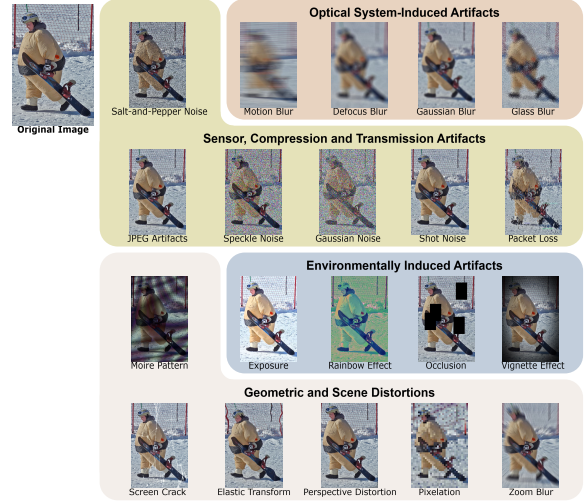


Figure 1. Our RoHOI dataset comprises 20 types of algorithmically generated corruptions, systematically categorized into four groups, i.e., *Optical system-induced artifacts*, *Sensor, compression and transmission artifacts*, *Environmentally induced artifacts*, and *Geometric and scene distortions*. Each corruption type has five levels of severity, leading to a total of 100 distinct corruptions. These corruptions simulate real-world degradation factors encountered in practical applications.

tricate relationships between human-object pairs by leveraging large-scale datasets and contextual information. Despite these advancements, such models remain highly sensitive to various real-world corruptions, e.g., occlusion, lighting variations, and environmental shifts, which hinder their robustness and limit practical deployment. For instance, minor corruptions can cause substantial drops in accuracy, which poses significant risks in safety-critical applications like autonomous driving or robotics. This sensitivity raises serious concerns about the robustness and reliability of these models in unpredictable environments. Ensuring robust and reliable HOI detection in diverse, complex corruptions remains an unsolved challenge.

Existing HOI detection methods [2, 57, 78] predominantly evaluate model performance in idealized, clean conditions, overlooking real-world robustness.

*Correspondence: kunyu.peng@kit.edu

This gap in the evaluation pipeline highlights the urgent need for a dedicated robustness benchmark. Such a benchmark can systematically evaluate model performance under diverse corruptions and perturbations, offering key insights into resilience and adaptability.

In this paper, we introduce **Robustness benchmark for HOI detection (RoHOI)**, systematically assessing HOI detection models under 20 diverse corruptions designed to simulate real-world conditions based on HICO-DET [3] and V-COCO [13] datasets and robustness-focused metrics including Mean Robustness Index (MRI) [18] and our novel Composite Robustness Index (CRI). RoHOI extends robustness evaluation beyond clean datasets, exposing model vulnerabilities and guiding future improvements. Through our evaluations of existing HOI detection methods on the newly proposed robustness test sets, we observe that their performance remains limited. This finding underscores the necessity of developing more robust HOI detection models to ensure greater reliability in real-world applications.

To mitigate the issue of performance degradation, we propose a Semantic-Aware Masking-based Progressive Learning (SAMPL) method, which effectively leverages both holistic and partial cues from the clean training set. Specifically, we utilize SAM [28] to identify HOI-relevant regions and subsequently apply a dynamic masking strategy with varying ratios. This approach enables the model to focus on both holistic and partial information, thereby enhancing its robustness throughout the optimization process. Our proposed learning strategy delivers superior performance in HOI detection, achieving state-of-the-art (SOTA) performance on clean test set while delivering substantial improvements in recognition accuracy under the evaluation with the proposed corruptions. This advancement highlights the model’s enhanced resilience and reliability in challenging real-world conditions for HOI detection. The main contributions of this paper are summarized as follows:

- We for the first time introduce a robustness benchmark specifically tailored for HOI detection. Our benchmark incorporates 20 distinct corruptions that closely mirror real-world challenges and a set of robustness-focused metrics.
- We propose a novel semantic-aware masking curriculum learning approach that adaptively guides the model to optimize learning on both holistic and partial information.
- SAMPL yields SOTA in terms of robustness, surpassing prior HOI models under both clean and corrupted conditions. Our benchmark establishes a comprehensive evaluation framework for robustness in HOI detection.

2. Related Work

2.1. Human Object Interaction Detection

Human-object interaction (HOI) detection [11, 14, 32, 47, 59, 65, 67, 69, 77, 81] seeks to automatically identify and interpret relationships between humans and objects in images. Existing approaches can be clustered into two major groups, which are *one-stage* and *two-stage* approaches.

Two-Stage HOI Detection. Two-stage methods [34, 51, 64, 80] rely on the detection results from the existing object detectors, *e.g.*, Faster R-CNN [52]. CNN-based HOI detection methods [51, 64, 80] are explored by the researchers in the early stage. Graph structures [58, 61, 64, 73, 80] are well explored in the past to construct knowledge relation reasoning to pursue better human object interaction detection. Wan *et al.* [59] proposed pose aware multi-level network for HOI task. Zhang *et al.* [74] proposed an unpaired transformer architecture to achieve a better capture of the human-object interaction relations. Li *et al.* [33] proposed integrating and decomposing networks for HOI detection.

One-stage HOI Detection. One-stage HOI detection approaches [70, 75] have gained traction due to their efficiency and end-to-end learning advantages over two-stage methods. Liao *et al.* [35] introduced PPDM, leveraging parallel point detection and matching for real-time HOI detection. Kim *et al.* [24] proposed UnionDet, introducing a union-level detector to directly predict interaction triplets. Zhong *et al.* [79] introduced a glance-and-gaze mechanism to adaptively model action-aware points and refine interaction predictions. Recent advancements in transformer-based architectures further improved one-stage HOI detection. Kim *et al.* [27] proposed MUREN, which incorporates relational context learning to refine interaction reasoning. Yuan *et al.* [70] introduced RLIPv2, integrating Asymmetric Language-Image Fusion (ALIF) for scalable relational pretraining, achieving SOTA performance. VLMs have also been explored to enhance HOI detection, improving semantic understanding and generalization across unseen interactions. Liu *et al.* [23] proposed VLM-HOI, leveraging large-scale vision-language models for improved generalization. Zhang *et al.* [30] introduced EZ-HOI, enhancing zero-shot HOI triplet prediction through VLM-based feature learning. Addressing robustness in HOI detection, Wang *et al.* [7] proposed UAHOI, integrating uncertainty estimation to improve stability under varying conditions.

Most existing works are evaluated on clean datasets without considering data corruptions. However, in real-world applications, HOI detection models encounter various challenges leading to significant performance degradation. To address this, we introduce the first robustness benchmark for HOI detection, incorporating 20 test-time corruptions.

2.2. Visual Robustness Benchmarks

Robustness is crucial for visual understanding as it ensures models can maintain high performance despite variations in environmental conditions, such as noise, occlusions, or lighting changes, which are common in real-world scenarios [1, 4, 15, 16, 22, 39, 40, 44, 46, 53, 54, 60, 63, 68, 71]. Researchers have constructed diverse robustness benchmarks to assess the capability of models coming from different visual understanding fields under diverse perturbations. Liu *et al.* [38] proposed ARES-Bench benchmark to evaluate the robustness of existing image classification methods under perturbations. Ishma *et al.* [21] constructed a large-scale benchmark for the visual question answer task. Hendrycks *et al.* [18] proposed ImageNet-C, a widely used benchmark assessing model robustness against common corruptions like noise, blur, and weather effects. Li *et al.* [31] proposed ImageNet-E to benchmark the model robustness in attribute editing field. Peng *et al.* [49] proposed new benchmark to assess robustness of existing one-shot skeleton based human action recognition models against occlusion perturbation. Chen *et al.* [9] constructed RoDLA to enable the evaluation of robust document layout analysis. However, none of the existing works focus on the robust evaluation of HOI detection methods. In this work, we open the vistas of the uncharted robust HOI detection area by constructing new RoHOI benchmark on two public HOI detection datasets and put forward the SAMPL method to achieve more reliable HOI detection performances.

3. Benchmark

3.1. Corruptions

To rigorously assess HOI detection robustness, we introduce our dedicated RoHOI benchmark, designed to evaluate model performance under structured real-world corruptions. While many corruptions in existing datasets [18], such as brightness and contrast shifts, are mitigated through standard augmentation, their weather-based effects (*e.g.*, synthetic snow and frost) often fail to capture real-world optical complexities. Our benchmark introduces **20** corruption types, categorized into four groups: *Optical system-induced (OS) artifacts*, *Sensor, compression, and transmission (SCT) artifacts*, *Environmentally induced (EI) artifacts*, and *Geometric and scene (G&S) distortions* (see Fig. 1). Each corruption is applied at **five** severity levels, enabling a fine-grained analysis of robustness under increasing degradation.

OS Artifacts degrade spatial clarity and obscure interaction details by distorting object boundaries. Our benchmark includes *motion blur (MB)*, *defocus blur (DB)*, and *Gaussian blur (GauB)*, which simulate degradation caused by camera movement, misfocus, and signal processing. We refine *glass blur (GB)* to better replicate distortions caused by

imaging through uneven or scratched glass surfaces.

SCT Artifacts stem from hardware limitations, lossy encoding, and data transmission errors. Alongside standard corruptions like *Gaussian noise (GauN)*, *shot noise (ShN)*, *salt-and-pepper noise (S&P)*, *JPEG artifacts (JPEG)*, and *speckle noise (SN)*, we introduce *packet loss (PL)*, which simulates data degradation due to incomplete transmissions.

EI Artifacts alter image quality due to external conditions. Extreme lighting variations cause *exposure (EXP)* distortion. The *rainbow effect (RE)* misaligns color channels, distorting object hues. *Occlusion (OCC)* removes critical visual information when foreign objects block key scene elements, while *vignette effect (VE)* creates uneven brightness, reducing visibility at image borders.

G&S Distortions alter spatial relationships and object proportions. *Moiré patterns (MP)* create artificial wave-like distortions in high-frequency textures. *Screen crack (SC)* introduce irregular fractures and glare artifacts, while *elastic transformation (ET)* warp object structures. *Perspective distortion (PD)* skews object shapes when captured at extreme angles. *Pixelation (PIX)* replaces fine details with block-like artifacts due to low-resolution rendering, and *zoom blur (ZB)* degrades object sharpness through rapid motion along the optical axis.

3.2. Datasets

To evaluate robustness under real-world corruptions, we use two widely adopted HOI detection datasets: HICO-DET and V-COCO. **HICO-DET** [62] contains 47,776 images with 600 interaction classes derived from 117 action classes and 80 object categories. Each image is annotated with human-object pairs and their corresponding interactions, making it a benchmark for evaluating diverse HOI scenarios. **V-COCO** [13] is a subset of MS-COCO [37] with 10,346 images, 16,199 human instances, 81 object categories and 29 verb classes. Unlike HICO-DET, which provides a fine-grained benchmark, V-COCO evaluates model performance on common human-object interactions. Evaluating these datasets under corruption provides a systematic robustness assessment beyond clean-image performance.

3.3. Baselines

To systematically evaluate the robustness of HOI detection models, we benchmark both two-stage and one-stage architectures, including transformer-based and vision-language pretraining approaches. Two-stage methods first detect objects before predicting interactions. We evaluate QPIC [56] and UPT [74], both of which use object detectors to extract human-object proposals before interaction classification. We include CDN [72], which refines interaction reasoning via a cascade structure, and DiffHOI [66], which leverages text-to-image diffusion priors to improve rare interaction recognition. One-stage methods directly predict

interactions without explicit object detection, improving efficiency. We evaluate FGAHOI [43], which enhances spatial alignment using fine-grained anchors, and QAHOI [5], which integrates query-based attention for interaction localization. Additionally, we include MUREN [27], which refines relational context modeling, and SOV-STG [6], which optimizes decoder attention for verb-object association. GEN-VLKT [36] incorporates visual-language pretraining to improve interaction recognition. RLIPv2 [70] incorporates region-language alignment for fine-grained interaction reasoning. Additionally, we develop SAMPL, which is built upon RLIPv2 and incorporates semantic-aware masking-based progressive learning. Our benchmark systematically evaluates these models across diverse corruption types and severity levels, providing a comprehensive assessment of HOI detection robustness.

3.4. Evaluation Metrics

We evaluate clean test set of HICO-DET [62] using mAP at Intersection over Union (IoU) 0.5 for all (Full), rare (<10 instances), and non-rare (≥ 10 instances) categories [70]. For clean test set of V-COCO [13], we use AP_{role} for interaction detection, with $AP_{\text{role}}^{\#1}$ for action recognition and $AP_{\text{role}}^{\#2}$ requiring object localization at IoU 0.5. To evaluate HOI detection performance on our robustness benchmark, we introduce two robustness-focused metrics: **Mean Robustness Index (MRI)** and **Composite Robustness Index (CRI)**. MRI, following the definition in prior work [18], measures average performance under corruptions but overlooks stability across severity levels. To address this, we propose CRI, which penalizes performance variance while normalizing against clean-set accuracy, ensuring models with consistent robustness are appropriately rewarded.

3.4.1. Mean Robustness Index (MRI)

MRI serves as a baseline measure of a model’s average performance across corruption types and severities:

$$\text{MRI} = \frac{1}{C} \sum_{c=1}^C \left(\frac{1}{L_c} \sum_{l=1}^{L_c} mAP_{c,l} \right), \quad (1)$$

where C denotes the number of corruption types, L_c represents the number of severity levels for the c -th corruption, and $mAP_{c,l}$ is the model’s performance at level l of corruption c . While MRI provides an overall robustness estimate, it does not account for performance fluctuations across corruption levels.

3.4.2. Composite Robustness Index (CRI)

To address MRI’s limitations, we propose CRI, which penalizes performance instability across corruption levels while normalizing against clean-set performance:

$$\text{CRI} = \frac{1}{C} \sum_{c=1}^C \left(\frac{\overline{mAP}_c}{mAP_{\text{clean}}} \cdot \frac{1}{\log(1 + \sigma_c) + 1} \right), \quad (2)$$

where \overline{mAP}_c is the mean mAP for corruption type c , and σ_c is the standard deviation across corruption levels. The clean-set performance mAP_{clean} is defined as mAP (Full) for HICO-DET and $AP_{\text{role}}^{\#2}$ for V-COCO, where $AP_{\text{role}}^{\#2}$ requires both action and object localization, with an IoU threshold of 0.5. The penalty term $\frac{1}{\log(1 + \sigma_c) + 1}$ reduces scores for models with high variance, ensuring that robustness accounts for both overall performance and stability.

By integrating absolute accuracy with degradation consistency, CRI favors models that maintain stable performance across corruption levels, mitigating the impact of abrupt performance drops. For completeness, we also report standard HICO-DET mAP and V-COCO role-based AP scores, following prior benchmarks (detailed in Supplementary).

4. Method

In this section, we present our novel approach, Semantic-Aware Masking-based Progressive Learning (SAMPL), which improves model optimization by enhancing both holistic and partial feature learning. This is achieved through dynamically masked inputs, with the mask generation guided by the SAM [28] to identify Regions Of Interest (ROI) in HOI detection. The adaptive progressive learning strategy adjusts the masking procedure automatically based on the model’s performance on the validation set and the recorded frequency, ensuring more robust feature learning. We will now provide a detailed explanation of the design of our approach.

SAM Guided HOI-Aware Semantic Masking (SAMSM).

Our goal is to maximize the utilization of the information provided by the clean training set to enhance the model’s robustness. This is achieved by ensuring that both holistic and partial cues are effectively extracted and learned, ultimately benefiting model optimization. By applying masks of varying scales to the semantic regions of interest in the image (*i.e.*, areas related to interacted objects and person areas), we assist the model in learning HOI cues within the restricted regions.

To implement this masking strategy, we use ground-truth bounding boxes and SAM-generated masks for instance-aware occlusions. Each object’s bounding box is processed by SAM to obtain a fine-grained segmentation mask M_b . To prevent reliance on instance contours, we apply random edge expansion, ensuring occlusion does not strictly follow the instance’s boundaries. Instead of naively occluding entire bounding boxes, we selectively mask regions within M_b while preserving surrounding contextual cues. This strategy prevents the model from relying solely on object appearance and encourages it to infer interactions based on partial information. During training, the masked pixels in the image are replaced with zero values.

Next, we define various severity levels for the mask to

Algorithm 1 SAMPL

Input: Severity levels of semantic aware masking: $\Omega = \{\omega_1, \omega_2, \omega_3, \omega_4\}$, initial threshold: τ_{init} , maximum epochs: T , HOI detection model: \mathcal{H}_θ .

Initialize: $N(\Omega) \leftarrow \mathbf{1}^{4 \times 1}$, $\Delta Q_{\text{max}} \leftarrow -\infty$, $p \leftarrow 2$.

```
1: for  $t = 1$  to  $T$  do
2:   Compute  $Q_\omega(t)$  for  $\omega \in \{\omega_1, \omega_p\}$  using  $\mathcal{H}_\theta$ .
3:   Get  $S_{\omega_p}(t) = \sum_i N(\omega_i) \cdot Q_{\omega_p}(t)$ . Get  $S_{\omega_1}(t) = N(\omega_1) \cdot Q_{\omega_1}(t)$ .
4:   Select severity level  $\omega^* = \arg \min_{\omega \in \{\omega_1, \omega_p\}} S_\omega(t)$ .
5:   if  $\omega^* \neq \omega_1$  then
6:     Compute  $\Delta Q(t) = \frac{Q_{\omega_p}(t) - Q_{\omega_p}(t-1)}{Q_{\omega_p}(t-1)}$ .
7:     Update  $\Delta Q_{\text{max}} = \max(\Delta Q_{\text{max}}, |\Delta Q(t)|)$ .
8:     Compute  $\tau(t) = \tau_{\text{init}} \cdot \frac{\Delta Q_{\text{max}}}{|\Delta Q(t)| + \epsilon}$ .
9:     if  $|\Delta Q(t)| < \tau(t)$  and  $p < 4$  then
10:       $p := p + 1$ . Train model on  $\omega_p$ .
11:       $N(\omega_p) := N(\omega_p) + 1$ .  $\Delta Q_{\text{max}} \leftarrow -\infty$ 
12:    else Train model on  $\omega^*$ .  $N(\omega_p) := N(\omega_p) + 1$ .
13:    end if
14:  else Train model on  $\omega_1$ .  $N(\omega_1) := N(\omega_1) + 1$ .
15:  end if
16: end for
```

obtain different partial cues from the original image. These severity levels are represented by $\Omega = \{\omega_1, \omega_2, \omega_3, \omega_4\}$, corresponding to clean, low, middle, and high levels. The clean level represents the original, unmasked data to support holistic feature learning. For the other three levels, cover ratios are determined to control the final height and width of the generated black box for semantic-aware masking, which can be denoted as $[r_\omega^w, r_\omega^h]$, where $\omega \in [\omega_2, \omega_3, \omega_4]$.

We then generate the mask for the severity level ω using the following equation:

$$\mathbf{M}_\omega^b = \Phi(\text{ConvHull}(\text{Dilation}(\mathbf{M}_b)), [r_\omega^w, r_\omega^h]), \quad (3)$$

In this process, we first apply binary dilation to the semantic mask \mathbf{M}_b , then compute the rectangular convex hull, and finally resize the resulting rectangular mask using the corresponding ratio $[r_\omega^w, r_\omega^h]$. The operation Φ refers to the resizing procedure that controls the mask size. The final mask, \mathbf{M}_ω^b , is the resulting mask that aids partial feature learning in our proposed robust training method.

Score Guided Progressive Feature Learning. To fully exploit the potential of the proposed SAM-guided semantic masks for maximizing HOI cue extraction, we introduce a novel score-guided progressive feature learning framework that incorporates a frequency memory bank across all severity levels.

Initially, training begins with the lowest severity level, while a memory bank is designed to track the utilization frequency of different severity levels. The perturbation level

is then progressively increased to a more challenging level based on the relative change in the evaluation metric between consecutive epochs. Notably, the severity level is only upgraded when the selected level differs from ω_1 . Let $\Delta Q(t)$ represent the relative change in the evaluation score on the validation set at epoch t :

$$\Delta Q(t) = \frac{Q_\omega(t) - Q_\omega(t-1)}{Q_\omega(t-1)}, \quad (4)$$

where $Q_\omega(t-1)$ is the evaluation metric for the current masking severity level in the previous epoch. To ensure stability, the perturbation level is upgraded when the magnitude of $\Delta Q(t)$ falls below a dynamically adjusted threshold $\tau(t)$:

$$\tau(t) = \tau_{\text{init}} \cdot \frac{\Delta Q_{\text{max}}}{|\Delta Q(t)| + \epsilon}, \quad (5)$$

where τ_{init} is the initial threshold, $\Delta Q_{\text{max}} = \max_{k \leq t} |\Delta Q(k)|$ is the maximum observed relative change in Q up to epoch t , and ϵ is a small constant to avoid division by zero.

The severity level l is updated as:

$$p := \begin{cases} p + 1 & \text{if } |\Delta Q(t)| < \tau(t) \text{ and } p < 4, \\ p & \text{otherwise.} \end{cases} \quad (6)$$

At epoch t , let $N(\omega)$ represent the number of times one severity level ω has been selected up to epoch t to serve as the aforementioned frequency memory bank. Let $Q_\omega(t)$ denote the validation performance for severity level ω at epoch t . The severity level score $S_\omega(t)$ is thereby defined as:

$$S_{\omega_p}(t) = \sum_i N(\omega_i) \cdot Q_{\omega_p}(t), \omega_i \in \Omega / \{\omega_1\}. \quad (7)$$

Then we obtain $S_{\omega_1} = N(\omega_1) \cdot Q_{\omega_1}(t)$. At each epoch, the next training severity level is chosen between the original data ω_1 (i.e., lowest severity level to achieve holistic feature learning) and ω_p . The selected severity level ω^* is determined as:

$$\omega^* = \arg \min_{\omega \in \{\omega_1, \omega_p\}} S_\omega(t). \quad (8)$$

The whole procedure is summarized in Alg. 1.

5. Experimental Results

5.1. Implementation Details

Our SAMPL method is built upon RLIPv2 [70] with a Swin-Tiny [41] backbone and has 214M trainable parameters. The backbone is pretrained on Visual Genome [29], MS-COCO [37] and Object365 [55], and the model is fine-tuned on the HICO-DET or V-COCO datasets. All experiments run on 4× A100 40GB GPUs using PyTorch 1.10.0

Method	Backbone	Pretrained	HICO-DET			MRI↑	CRI↑	V-COCO		MRI↑	CRI↑
			Full	Rare	Non-Rare			AP ^{#1} _{role}	AP ^{#2} _{role}		
Two-Stage methods											
QPIC [56]	R50	✗	29.07	21.85	31.23	13.13	0.21	58.80	60.98	30.04	0.19
QPIC [56]	R101	✗	29.90	23.92	31.69	14.45	0.22	58.27	60.74	32.05	0.19
UPT [74]	R50	✗	31.66	25.94	33.36	17.77	0.23	58.96	64.47	35.92	0.15
UPT [74]	R101	✗	32.31	28.55	33.44	17.44	0.24	60.70	66.20	33.80	0.14
CDN-B [72]	R50	✗	31.78	27.55	33.05	15.41	0.22	62.29	64.42	34.30	0.19
CDN-L [72]	R101	✗	32.07	27.19	33.53	17.05	0.24	63.91	65.89	37.65	0.20
DiffHOI [66]	R50	✗	34.41	31.07	35.40	21.09	0.23	-	-	-	-
One-Stage methods											
FGAHOI [43]	Swin-T	✓	29.81	22.17	32.09	16.05	0.22	-	-	-	-
GEN-VLKT-S [36]	R50	✗	33.75	29.25	35.10	17.01	0.22	62.41	64.46	34.69	0.19
GEN-VLKT-L [36]	R101	✗	34.95	31.18	36.08	18.93	0.23	63.58	65.93	37.45	0.20
QAHOI [5]	Swin-T	✓	28.47	22.44	30.27	15.07	0.25	58.23	58.70	29.33	0.20
SOV-STG-S [6]	R50	✗	33.80	29.28	35.15	16.94	0.22	62.88	64.47	34.40	0.20
MUREN [27]	R50	✓	32.88	28.70	34.13	16.32	0.23	68.10	69.88	37.10	0.18
RLIPv2-ParSeDA [70]	Swin-T	✓	38.60	33.66	40.07	24.58	0.28	68.83	70.76	45.05	0.24
SAMPL (ours)	Swin-T	✓	39.16	33.89	40.73	24.25	0.29	69.04	71.13	48.83	0.27

Table 1. Comparison of HOI detection methods on HICO-DET [62] and V-COCO [13]. Results on HICO-DET are reported on Full, Rare, and Non-Rare sets, while results on V-COCO are evaluated using AP $^{#1}$ _{role} and AP $^{#2}$ _{role}. MRI and CRI represent the Mean Robustness Index and Composite Robustness Index, respectively, measuring model resilience under corruption. Backbone architectures include ResNet-50 (R50), ResNet-101 (R101) [17], and Swin-Tiny (Swin-T) [41].

and CUDA 11.3. We use the AdamW [42] optimizer with an initial learning rate of $1e-4$, while the backbone and text encoder are trained with a lower learning rate of $1e-5$. A linear warmup strategy is applied for the first $10k$ steps, followed by a cosine decay schedule. We apply a weight decay of $1e-4$, and the batch size is 2 per GPU, with gradient accumulation over 2 steps to mitigate memory constraints. Training is conducted for 100 epochs. Following RLIPv2 settings, we adopt cross-entropy loss for object classification, focal loss for verb classification, and L1 + GIoU loss for bounding box regression. Additionally, KL divergence is used to regularize the latent space. The encoder consists of 6 layers, whereas the decoder contains 3 layers. For the dynamic severity adjustment mechanism, we set the initial threshold as $\tau_{\text{init}} = 0.15$ and $\epsilon = 10^{-6}$.

5.2. Analysis of the Benchmark

Table 1 presents the performance comparison between SAMPL and existing one-stage and two-stage HOI detection methods on HICO-DET [62] and V-COCO [13] datasets. SAMPL surpasses RLIPv2 [70], improving MRI by 3.78 and CRI by 12.5% on V-COCO, demonstrating superior robustness against visual degradations. On HICO-DET, SAMPL achieves a 3.6% higher CRI while maintaining comparable MRI, ensuring strong generalization without compromising clean-set accuracy. These results are further supported by Fig. 2, where SAMPL consistently outperforms two-stage and one-stage baselines across all 4 corruption categories in the RoHOI benchmark, achieving the highest MRI in each group and demonstrating improvements over the current SOTA model at every severity level

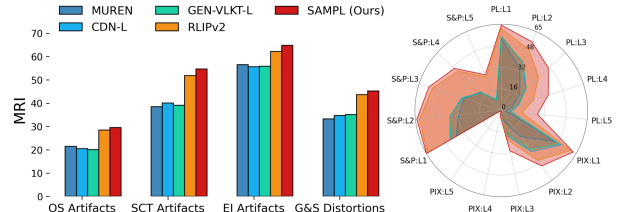


Figure 2. Comparison of SAMPL with strong two-stage and one-stage baselines trained on V-COCO under RoHOI benchmarks. The left bar chart groups performance by corruption categories, while the right radar chart compares models across five severity levels for three corruptions. Corruptions are denoted as Abbreviation, *i.e.*, $L\gamma$, where γ represents the severity level. Details are shown in Sec. 3.1.

(detailed in the supplementary). While extreme noise levels still pose challenges, SAMPL significantly improves robustness compared to prior methods. These results highlight SAMPL’s effectiveness in enhancing HOI detection under corrupted conditions through our proposed semantic-aware masking and progressive learning. Through a comprehensive analysis of representative HOI models, we derive the following key findings.

Observation 1: Large-scale vision-language pretraining significantly enhances the robustness of transformer-based models. According to the experiments conducted both on the clean test set and our perturbed test set on the two datasets, shown in Table 1, we observe that transformer-based architectures exhibit varying levels of robustness depending on their pretraining strategies. RLIPv2 [70], which leverages large-scale multimodal pretraining, achieves substantially higher robustness scores in contrast to GEN-

Perturbation Type	V-COCO		MRI↑	CRI↑
	AP#1_role	AP#2_role		
RLIPv2-ParSeDA+SAMSM	68.27	70.24	48.20	0.27
RLIPv2-ParSeDA+AGNP	68.33	70.51	44.74	0.24
RLIPv2-ParSeDA+RPP	67.69	69.64	47.59	0.25

Table 2. Ablation study on various perturbation strategies during training. We evaluate SAM-guided HOI-aware Semantic Masking (SAMSM), Adaptive Gaussian Noise Perturbation (AGNP), and Randomized Pixelation Perturbation (RPP) on the V-COCO.

VLKT [36], SOV-STG [6] and other transformer-based methods. This suggests that large-scale vision-language pretraining provides a more structured relational feature space, mitigating feature drift and localization sensitivity in HOI detection tasks. Furthermore, two-stage models that utilize pretrained detector backbone, *e.g.*, UPT [74], show only moderate robustness improvements, highlighting the importance of diverse relational supervision beyond object-centric datasets.

Observation 2: Object localization strategies dictate robustness in two-stage architectures. Two-stage methods show varying robustness across different object localization strategies. Region-proposal-based models [72] achieve high clean-set accuracy but degrade under corruption due to error propagation in localization. In contrast, query-based methods [74] adapt object representations dynamically, enhancing robustness on HICO-DET. However, this advantage diminishes on V-COCO, where UPT with a larger backbone exhibits lower CRI than CDN [72] with a smaller backbone, likely due to V-COCO’s limited interaction diversity. This suggests that query-based detection benefits from diverse datasets but struggles with constrained interaction distributions.

Observation 3: Interaction representation entanglement amplifies robustness degradation under perturbations. Models with tightly coupled interaction representations achieve higher clean-set accuracy but are more prone to corruption due to feature distortion propagation. MUREN [27], with multi-level relational context learning, suffers the largest MRI and CRI drop, showing that excessive entanglement weakens robustness. Similarly, GEN-VLKT-L’s global self-attention leads to greater degradation than CDN-L’s decoupled interaction classification, while QAHOI’s [5] adaptive query-based approach improves robustness by dynamically refining predictions. This underscores a key trade-off: stronger feature coupling boosts accuracy but reduces resilience to corruptions.

Observation 4: Dataset interaction diversity directly influences robustness generalization. Models trained on HIO-DET achieve higher MRI and CRI than V-COCO-trained models due to greater interaction diversity, enhancing resilience. However, SAMPL shows stronger robustness gains on V-COCO, as its progressive learning strategy compensates for dataset limitations, achieving comparable

Cover Ratios	V-COCO		MRI↑	CRI↑
	AP#1_role	AP#2_role		
40%/50%/60%	69.04	71.13	48.83	0.27
40%/60%/70%	68.51	70.53	48.44	0.27
50%/60%/80%	68.21	70.29	48.26	0.27
50%/70%/80%	68.52	70.45	45.72	0.22

Table 3. Ablation study on training with different severity level combinations. SAMSM masks each instance based on 40%–80% of its bounding box height and width, using three candidate levels during training.

robustness with less data and fewer iterations. This underscores the importance of diverse interactions for general robustness and adaptive training for faster improvements in smaller datasets. Structural design considerations in both architectures and training paradigms are crucial for balancing recognition accuracy and robustness in real-world applications.

5.3. Analysis of the Ablation Study

To investigate the impact of perturbation-based training on model robustness, we conduct a series of ablation experiments on the V-COCO dataset. The results, presented in Tables 2 and 3, analyze the effects of different perturbation types and perturbation level settings on model performance. **Ablation of the Semantic-Aware Masking:** Table 2 evaluates three perturbation strategies applied independently during training, excluding our progressive learning method to isolate their direct impact. *SAM-guided HOI aware Semantic Masking (SAMSM)* is applied in 50% of training epochs, occluding instance’s regions while preserving contextual cues. *Adaptive Gaussian Noise Perturbation (AGNP)* introduces feature-level noise with a 50% probability, while *Randomized Pixelation Perturbation (RPP)* pixelates input images with the same probability as data augmentation. SAMSM achieves the highest MRI and CRI scores, suggesting that structured occlusions enhance robustness by enforcing relational reasoning under missing object regions. Unlike AGNP, which perturbs latent features without spatial structure, SAMSM provides localized challenges that align with real-world occlusions. Despite expectations that RPP would improve robustness—given that *pixelation* causes the most significant performance drop in baseline corruption tests (as shown in Fig. 4)—its randomized nature indiscriminately distorts both essential and redundant information, making adaptation less effective. These results suggest that robustness in HOI detection benefits more from structured perturbations that challenge object-awareness rather than indiscriminate degradations that introduce confounding artifacts.

Effect of Perturbation Levels: Table 3 analyzes the impact of masking severity on robustness. SAMSM occludes 40%–80% of each instance’s bounding box, with the 40%/50%/60% setting achieving the best trade-off, max-



Figure 3. Qualitative comparison of HOI detection under corruption between SAMPL (ours) and RLIPv2 [70]. The first row shows uncorrupted images, while the second and third rows present SAMPL and RLIPv2 results on corrupted images. Missed predictions are in dashed red, false interactions in red, and correct ones in blue.

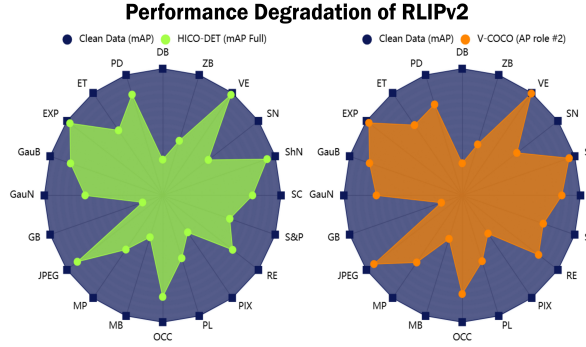


Figure 4. Performance degradation of RLIPv2 [70] on HICO-DET [62] and V-COCO [13] under RoHOI. The left radar chart shows the relative mAP (Full) drop on HICO-DET, while the right shows the decline in $AP_{role}^{#2}$ on V-COCO. Clean dataset performance serves as a reference, with shaded areas indicating corruption impact, with abbreviations mentioned in Sec. 3.1.

imizing MRI and CRI while maintaining competitive AP scores. Moderate occlusions enhance feature learning via contextual cues, while excessive masking ($> 70\%$) disrupts spatial structures, reducing discriminative capacity. These findings emphasize the need for controlled occlusions that challenge models without excessive information loss.

Overall, perturbation-based training enhances HOI detection robustness, with SAMSM proving most effective by balancing global context preservation and local feature resilience. Moderate perturbation achieves optimal robustness without sacrificing clean-data accuracy.

5.4. Analysis of the Qualitative Results

Fig. 3 compares SAMPL with RLIPv2 [70] under various corruptions, demonstrating SAMPL’s superior robustness in the first four cases while highlighting shared failure patterns in the last two. Under *Screen Crack* corruption (Column

1), SAMPL accurately detects occluded background persons and their “ride” interactions, whereas RLIPv2 misses smaller subjects, indicating SAMPL’s stronger resilience to fragmented textures. In *Pixelation* noise (Column 2), our method correctly recognizes “work on computer”, while RLIPv2 misclassifies it as “cut”, suggesting greater robustness against structured perturbations. Under *Salt-and-Pepper Noise* (Column 3), RLIPv2 confuses “sit” with “ride”, likely due to the presence of an adjacent animal, whereas SAMPL maintains stable interaction recognition, reducing reliance on object-centric biases. In *Moiré Pattern* (Column 4) corruption, RLIPv2 incorrectly detects “talk on phone”, possibly due to moiré-induced distortions interfering with high-frequency texture recognition. However, under high-severity *Glass Blur* (Column 5) and *Moiré Pattern* corruption (Column 6), both models misclassify actions as “surf” or “talk on phone”, potentially because V-COCO’s limited action categories encourage overfitting to common interactions under extreme degradation rather than a traditional long-tail distribution issue. These results highlight SAMPL’s advantages in structured occlusions and texture-based corruptions. However, both models remain vulnerable under severe degradations, where dataset priors dominate predictions.

6. Conclusion

In this paper, we introduced RoHOI, the first robustness benchmark for HOI detection, evaluating models under 20 real-world perturbations. Our analysis shows that existing models suffer significant degradation, highlighting the need for more robust approaches. To address this, we propose SAMPL, a Semantic-Aware Masking-based Progressive Learning method that utilizes SAM-generated region-

aware masks and dynamically adjusts masking severity. SAMPL enhances robustness while maintaining high accuracy on clean datasets, outperforming state-of-the-art methods. By bridging the gap between clean-data performance and real-world robustness, our work advances reliable and adaptable HOI detection models for practical use.

A. Social Impact and Limitations

Social Impact: We introduce RoHOI, the first benchmark for assessing HOI detection robustness under real-world corruptions, incorporating 20 degradation types to bridge the gap between theoretical advancements and deployment. Robust HOI detection is crucial for safety-critical applications, yet existing models struggle with occlusions and noise. To address this, we propose SAMPL, a semantic-aware masking and progressive learning approach that enhances resilience to distortions, outperforming SOTA models in both clean and corrupted settings. However, challenges remain, including biased predictions and disparities across interaction categories, underscoring the need for further research in bias mitigation, domain adaptation, and fairness-aware robustness.

Limitations: RoHOI focuses on synthetic corruptions but may not fully capture real-world domain shifts like scene-specific occlusions and adversarial attacks, highlighting the need for real-world corrupted data. While SAMPL improves robustness, it still struggles with severe distortions (*e.g.*, moire patterns, glass blur), indicating the need for further architectural advancements.

B. Standard HOI Evaluation Metrics

This section provides a detailed explanation of the evaluation metrics used for HICO-DET [64] and V-COCO [13] in our main paper. These include the standard mAP metrics for HICO-DET and AP_{role} variations for V-COCO.

B.1. mAP(Full, Rare, Non-Rare)

We evaluate models on HICO-DET using the standard mAP under an IoU threshold of 0.5. The reported metrics include mAP (Full), which evaluates all 600 HOI categories; mAP (Rare), assessing performance on low-frequency categories with fewer than 10 instances; and mAP (Non-Rare), focusing on categories with at least 10 instances.

B.2. $AP_{role}^{#1}$ and $AP_{role}^{#2}$

We evaluate V-COCO using AP_{role} , which measures interaction detection accuracy. $AP_{role}^{#1}$ assesses action recognition without strict role object localization. $AP_{role}^{#2}$ requires both action and object localization, with an IoU threshold of 0.5.

C. Corruption Types in the Dataset

Building upon the general introduction in the main text, this section provides a more detailed breakdown of the 20 corruption types used in our RoHOI benchmark.

C.1. Optical System-Induced (OS) Artifacts

Motion Blur (MB): Blur caused by the relative motion between the camera and the scene during exposure. This artifact is included as it commonly occurs in dynamic scenes or when handheld cameras are used. Severity levels are generated by increasing the kernel size of a linear motion blur filter. (Details shown in Table 6, row 1.)

Defocus Blur (DB): Blur resulting from the lens being improperly focused on the subject. This noise reflects the limitations of camera focus systems, particularly in low-light or high-speed scenarios. Severity levels are controlled by varying the radius of a circular point spread function (PSF). (Details shown in Fig. 6, row 2.)

Gaussian Blur (GauB): Blur due to scattering or inherent optical limitations of the lens. This artifact simulates the diffusion of light caused by imperfect optical surfaces or aperture settings. Severity levels are adjusted by increasing the standard deviation of the Gaussian kernel. (Details shown in Fig. 6, row 3.)

Glass Blur (GB): Blur introduced when imaging through imperfect or contaminated transparent materials (*e.g.*, glass or plastic). This type is included to represent common real-world challenges such as photographing through windows or protective covers. Severity levels are generated by applying iterative small displacements and local blurring. (Details shown in Fig. 6, row 4.)

C.2. Sensor, Compression and Transmission (SCT) Artifacts

Salt-and-Pepper Noise (S&P): Discrete black-and-white pixel noise caused by sensor malfunction or transmission errors. This represents rare but impactful noise patterns in hardware-limited imaging systems. Severity levels are generated by increasing the probability of random pixel corruption. (Details shown in Fig. 6, row 1.)

JPEG Artifacts (JPEG): Blocky or blurry artifacts resulting from lossy image compression, which are used to evaluate model robustness to low-quality image formats frequently encountered in data storage and transmission. Severity levels are controlled by progressively reducing the JPEG quality factor. (Details shown in Fig. 6, row 2.)

Speckle Noise (SN): Speckle noise resembles the grainy texture seen on old printed photos or low-quality digital images taken in dim lighting. At lower severity levels, it appears as faint specks of dust on a camera lens, barely noticeable unless viewed closely. As severity increases, the noise becomes more pronounced, resembling the rough texture of sandpaper or the graininess of a poorly printed newspaper.

Model	MB	DB	GauB	GB	GauN	ShN	S&P	JPEG	SN	PL	EXP	RE	OCC	VE	MP	SC	ET	PD	PIX	ZB
CDN-L [72]	15.38	10.12	48.73	7.56	41.67	60.92	28.78	56.89	24.24	28.18	64.67	41.06	49.75	67.07	30.67	44.30	37.33	50.79	22.39	22.45
GEN-VLKT-L [36]	14.64	9.90	48.27	7.74	40.50	60.63	28.37	56.31	20.40	28.52	64.94	40.48	50.48	67.48	32.42	44.21	38.27	51.15	21.11	23.24
MUREN [27]	15.71	12.10	51.08	6.77	41.65	62.59	26.08	56.32	20.46	23.89	66.65	38.55	51.78	69.12	25.63	44.36	38.79	52.34	15.97	22.22
RLIPv2-ParSeDA [70]	25.31	17.84	57.82	12.99	50.91	66.72	50.58	64.68	40.11	38.34	68.39	55.99	54.61	69.82	45.93	59.14	48.14	53.01	26.12	29.73
SAMPL (Ours)	26.63	19.03	58.56	13.87	52.46	68.06	52.66	65.81	42.24	46.69	69.22	57.31	62.04	70.77	47.89	60.72	48.99	53.21	29.90	30.49

Table 4. Comparison of MRI scores between our SAMPL method and the best-performing one-stage and two-stage HOI detection models on the RoHOI benchmark. The table presents results across 20 corruption types, evaluating model robustness under diverse corruptions. Corruption abbreviations follow the definitions provided in the main paper.







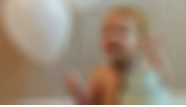









	Level 1	Level 2	Level 3	Level 4	Level 5
Motion Blur (MB)					
Defocus Blur (DB)					
Gaussian Blur (GauB)					
Glass Blur (GB)					

Table 5. Visual examples of Optical System (OS)-Induced artifacts across severity levels.

At the highest severity levels, the effect is akin to heavy rain blurring a car windshield, significantly degrading image clarity. (Details shown in Fig. 6, row 3.)

Gaussian Noise (GauN): Additive noise caused by sensor imperfections such as thermal noise or quantization errors. This is a ubiquitous noise model, reflecting baseline sensor limitations in most imaging devices. Severity levels are determined by progressively increasing the noise standard deviation. (Details shown in Fig. 6, row 4.)

Shot Noise (ShN): Random variations in pixel intensity caused by photon-counting statistics during exposure. This noise type represents the fundamental physical limits of image sensors in low-light conditions. Severity levels are controlled by adjusting the scale of the Poisson-distributed noise. (Details shown in Fig. 6, row 5.)

Packet Loss (PL): Missing or distorted image regions caused by data corruption during transmission. This noise simulates real-world challenges in wireless or network-based imaging systems. Severity levels are generated by increasing the number and size of corrupted or duplicated regions. (Details shown in Fig. 6, row 6.)

C.3. Environmentally Induced (EI) Artifacts

Exposure Artifacts (EXP): Loss of image details caused by underexposure or overexposure due to extreme lighting conditions. Higher severity levels increase the intensity of overexposure (bright regions saturate) or underexposure (dark regions lose details), leading to stronger visual degradation. This type is included to represent real-world challenges in scenes with poor or uncontrolled lighting. (Details shown in Fig. 7, row 1.)

Rainbow Effect (RE): Typically caused by the interaction between the projection system’s optical components (e.g., color wheels in DLP projectors) and the camera sensor. As severity increases, the color distortion becomes more pronounced, with broader and more intense rainbow bands appearing across the image, significantly altering local color distribution. This noise enables the evaluation of model robustness against chromatic distortions, particularly in scenes involving projected displays and reflective surfaces. (Details shown in Fig. 7, row 2.)

Occlusion (OCC): Partial obstruction of the field of view by external objects. Increasing severity levels introduce randomly placed black rectangular occlusions of varying sizes, progressively removing more contextual information from












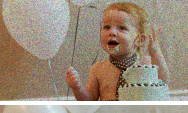
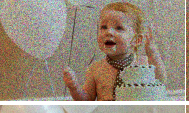






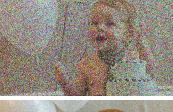










	Level 1	Level 2	Level 3	Level 4	Level 5
Salt-and-Pepper Noise (S&P)					
JPEG Artifact (JPEG)					
Speckle Noise (SN)					
Gaussian Noise (GauN)					
Shot Noise (ShN)					
Packet Loss (PL)					

Table 6. Visual examples of Sensor, Compression and Transmission (SCT) artifacts across severity levels.





















	Level 1	Level 2	Level 3	Level 4	Level 5
Exposure (EXP)					
Rainbow Effect (RE)					
Occlusion (OCC)					
Vignette Effect (VE)					

Table 7. Visual examples of Environmentally Induced (EI) artifacts across severity levels.

the image. This is a critical inclusion as occlusions are prevalent in crowded or dynamic environments. (Details shown in Fig. 7, row 3.)

Vignette Effect (VE): Gradual darkening at the edges of an image caused by lens design or aperture settings. With higher severity, the vignette effect has darker and wider peripheral regions, increasingly suppressing details in the outer parts of the image. This type represents a common optical limitation that affects peripheral details in wide-field

imaging. (Details shown in Fig. 7, row 4.)

C.4. Geometric and Scene (G&S) Distortions

Moire Pattern (MP): Interference patterns resulting from fine texture overlap with the camera’s pixel grid (e.g., fabric or screens). This artifact captures the challenges posed by imaging repetitive textures or high-frequency patterns. Severity levels adjust the density and contrast of the interference patterns. (Details shown in Fig. 8, row 1.)



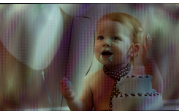














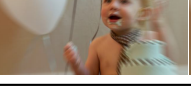
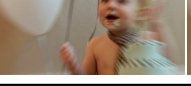
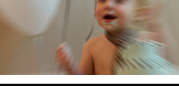
	Level 1	Level 2	Level 3	Level 4	Level 5
Moire Pattern (MP)					
Screen Crack (SC)					
Elastic Transform (ET)					
Perspective Distortion (PD)					
Pixelation (PIX)					
Zoom Blur (ZB)					

Table 8. Visual examples of Geometric and Scene (G&S) Distortions across severity levels.

Screen Crack Artifacts (SC): Visual obstructions or patterns caused by photographing through cracked or damaged surfaces. This type is included to reflect realistic scenarios where images are captured through broken screens or fractured glass. Higher severity levels introduce progressively denser and larger crack patterns, further obscuring the image. (Details shown in Fig. 8, row 2.)

Elastic Transform (ET): Non-linear distortions caused by perspective changes, material deformations, or uneven air density. This artifact represents challenges encountered in scenes with flexible or moving objects. Higher severity levels correspond to greater displacement magnitudes, leading to noticeable warping. (Details shown in Fig. 8, row 3.)

Perspective Distortion (PD): This artifact simulates geometric distortions from lens imperfections, such as barrel and pincushion distortion. Severity is increased by applying progressively stronger transformation matrices, exaggerating the curvature and altering the perceived structure of objects. (Details shown in Fig. 8, row 4.)

Pixelation (PIX): Blocky appearance due to low resolution or excessive digital zoom. This represents a key limitation in devices with constrained sensor capabilities or in images subjected to aggressive downscaling. Higher severity levels result in coarser pixel blocks, significantly reducing image detail. (Details shown in Fig. 8, row 5.)

Zoom Blur (ZB): Radial blur caused by rapid changes in focal length during image capture. Zoom blur is simulated

by iteratively applying slight scaling transformations and averaging the results to create a progressive radial blur effect. Higher severity levels increase both the scaling intensity and the number of blended layers, leading to a stronger blur radiating outward from the center. This method ensures a smooth and natural-looking zoom effect without abrupt artifacts. (Details shown in Fig. 8, row 6.)

C.5. Purpose of Inclusion

These noise types are selected to comprehensively represent real-world scenarios that affect image quality, ranging from optical and sensor limitations to environmental and dynamic scene factors. Their inclusion ensures the dataset’s relevance for evaluating model robustness in diverse and realistic conditions.

D. Benchmark Results on Corruption Types

Table 4 presents the MRI scores of our SAMPL method compared to the strongest one-stage and two-stage HOI detection baselines on the RoHOI benchmark. SAMPL consistently outperforms prior methods across all 20 corruption types, achieving the highest scores in every category. Notably, our approach shows significant improvements in handling severe degradations such as pixelation and packet loss, demonstrating enhanced robustness. These results validate the effectiveness of our SAMPL strategy in improving model resilience against real-world corruptions.

References

- [1] Bang An, Mucong Ding, Tahseen Rabbani, Aakriti Agrawal, Yuancheng Xu, Chenghao Deng, Sicheng Zhu, Abdirisak Mohamed, Yuxin Wen, Tom Goldstein, and Furong Huang. Benchmarking the robustness of image watermarks. In *ICML*, 2024. 3
- [2] Yichao Cao, Qingfei Tang, Xiu Su, Song Chen, Shan You, Xiaobo Lu, and Chang Xu. Detecting any human-object interaction relationship: Universal HOI detector with spatial prompt learning on foundation models. In *NeurIPS*, 2023. 1
- [3] Yu-Wei Chao, Yunfan Liu, Xieyang Liu, Huayi Zeng, and Jia Deng. Learning to detect human-object interactions, 2018. 2
- [4] Prithvijit Chattopadhyay, Judy Hoffman, Roozbeh Mottaghi, and Aniruddha Kembhavi. RobustNav: Towards benchmarking robustness in embodied navigation. In *ICCV*, 2021. 3
- [5] Junwen Chen and Keiji Yanai. QAHOI: Query-based anchors for human-object interaction detection. In *MVA*, 2023. 4, 6, 7
- [6] Junwen Chen, Yingcheng Wang, and Keiji Yanai. Focusing on what to decode and what to train: Efficient training with HOI split decoders and specific target guided denoising. *arXiv preprint arXiv:2307.02291*, 2023. 4, 6, 7
- [7] Mu Chen, Minghan Chen, and Yi Yang. UAHOI: Uncertainty-aware robust interaction learning for HOI detection. *CVIU*, 2024. 2
- [8] Yangyi Chen, Karan Sikka, Michael Cogswell, Heng Ji, and Ajay Divakaran. DRESS: Instructing large vision-language models to align and interact with humans via natural language feedback. In *CVPR*, 2024. 1
- [9] Yufan Chen, Jiaming Zhang, Kunyu Peng, Junwei Zheng, Ruiping Liu, Philip Torr, and Rainer Stiefelhagen. RoDLA: Benchmarking the robustness of document layout analysis models. In *CVPR*, 2024. 3
- [10] Mihai Dogariu, Liviu-Daniel Stefan, Mihai Gabriel Constantin, and Bogdan Ionescu. Human-object interaction: Application to abandoned luggage detection in video surveillance scenarios. In *COMM*, 2020. 1
- [11] Hao-Shu Fang, Jinkun Cao, Yu-Wing Tai, and Cewu Lu. Pairwise body-part attention for recognizing human-object interactions. In *ECCV*, 2018. 2
- [12] Jianjun Gao, Kim-Hui Yap, Kejun Wu, Duc Tri Phan, Kratika Garg, and Boon Siew Han. Contextual human object interaction understanding from pre-trained large language model. In *ICASSP*, 2024. 1
- [13] Saurabh Gupta and Jitendra Malik. Visual semantic role labeling. *arXiv preprint arXiv:1505.04474*, 2015. 1, 2, 3, 4, 6, 8, 9
- [14] Tanmay Gupta, Alexander Schwing, and Derek Hoiem. No-frills human-object interaction detection: Factorization, layout encodings, and training techniques. In *ICCV*, 2019. 2
- [15] Xiaoshuai Hao, Mengchuan Wei, Yifan Yang, Haimei Zhao, Hui Zhang, Yi Zhou, Qiang Wang, Weiming Li, Lingdong Kong, and Jing Zhang. Is your HD map constructor reliable under sensor corruptions? In *NeurIPS*, 2024. 3
- [16] Xiaoshuai Hao, Guanqun Liu, Yuting Zhao, Yuheng Ji, Mengchuan Wei, Haimei Zhao, Lingdong Kong, Rong Yin, and Yu Liu. MSC-Bench: Benchmarking and analyzing multi-sensor corruption for driving perception. *arXiv preprint arXiv:2501.01037*, 2025. 3
- [17] Kaiming He, Xiangyu Zhang, Shaoqing Ren, and Jian Sun. Deep residual learning for image recognition. In *CVPR*, 2016. 6
- [18] Dan Hendrycks and Thomas G. Dietterich. Benchmarking neural network robustness to common corruptions and perturbations. In *ICLR*, 2019. 2, 3, 4
- [19] Zhi Hou, Baosheng Yu, Yu Qiao, Xiaojiang Peng, and Dacheng Tao. Affordance transfer learning for human-object interaction detection. In *CVPR*, 2021. 1
- [20] Zhi Hou, Baosheng Yu, Yu Qiao, Xiaojiang Peng, and Dacheng Tao. Detecting human-object interaction via fabricated compositional learning. In *CVPR*, 2021. 1
- [21] Md Farhan Ishmam, Ishmam Tashdeed, Talukder Asir Saadat, Md. Hamjajul Ashmafee, Abu Raihan Mostofa Kamal, and Md. Azam Hossain. Visual robustness benchmark for visual question answering (VQA). *arXiv preprint arXiv:2407.03386*, 2024. 3
- [22] Christoph Kamann and Carsten Rother. Benchmarking the robustness of semantic segmentation models. In *CVPR*, 2020. 3
- [23] Donggook Kang, Dasol Jeong, Hyunmin Lee, Sangwoo Park, Hasil Park, Sunkyu Kwon, Yeongjoon Kim, and Joonki Paik. VLM-HOI: Vision language models for interpretable human-object interaction analysis. *arXiv preprint arXiv:2411.18038*, 2024. 2
- [24] Bumsoo Kim, Taeho Choi, Jaewoo Kang, and Hyunwoo J Kim. UnionDet: Union-level detector towards real-time human-object interaction detection. In *ECCV*, 2020. 2
- [25] Bumsoo Kim, Junhyun Lee, Jaewoo Kang, Eun-Sol Kim, and Hyunwoo J. Kim. HOTR: End-to-end human-object interaction detection with transformers. In *CVPR*, 2021. 1
- [26] Bumsoo Kim, Jonghwan Mun, Kyoung-Woon On, Minchul Shin, Junhyun Lee, and Eun-Sol Kim. MSTR: Multi-scale transformer for end-to-end human-object interaction detection. In *CVPR*, 2022. 1
- [27] Sanghyun Kim, Deunsol Jung, and Minsu Cho. Relational context learning for human-object interaction detection. In *CVPR*, 2023. 2, 4, 6, 7, 10
- [28] Alexander Kirillov, Eric Mintun, Nikhila Ravi, Hanzi Mao, Chloé Rolland, Laura Gustafson, Tete Xiao, Spencer Whitehead, Alexander C. Berg, Wan-Yen Lo, Piotr Dollár, and Ross B. Girshick. Segment anything. In *ICCV*, 2023. 2, 4
- [29] Ranjay Krishna, Yuke Zhu, Oliver Groth, Justin Johnson, Kenji Hata, Joshua Kravitz, Stephanie Chen, Yannis Kalantidis, Li-Jia Li, David A. Shamma, Michael S. Bernstein, and Li Fei-Fei. Visual genome: Connecting language and vision using crowdsourced dense image annotations. *International Journal of Computer Vision*, 2017. 5
- [30] Qinqian Lei, Bo Wang, and Robby Tan. EZ-HOI: VLM adaptation via guided prompt learning for zero-shot HOI detection. In *NeurIPS*, 2024. 2
- [31] Xiaodan Li, Yuefeng Chen, Yao Zhu, Shuhui Wang, Rong Zhang, and Hui Xue. ImageNet-E: Benchmarking neural network robustness via attribute editing. In *CVPR*, 2023. 3

- [32] Yong-Lu Li, Siyuan Zhou, Xijie Huang, Liang Xu, Ze Ma, Hao-Shu Fang, Yanfeng Wang, and Cewu Lu. Transferable interactiveness knowledge for human-object interaction detection. In *CVPR*, 2019. 2
- [33] Yong-Lu Li, Xinpeng Liu, Xiaoqian Wu, Yizhuo Li, and Cewu Lu. HOI analysis: Integrating and decomposing human-object interaction. In *NeurIPS*, 2020. 2
- [34] Zhijun Liang, Junfa Liu, Yisheng Guan, and Juan Rojas. Visual-semantic graph attention networks for human-object interaction detection. In *ROBIO*, 2021. 2
- [35] Yue Liao, Si Liu, Fei Wang, Yanjie Chen, Chen Qian, and Jiashi Feng. PPDM: Parallel point detection and matching for real-time human-object interaction detection. In *CVPR*, 2020. 2
- [36] Yue Liao, Aixi Zhang, Miao Lu, Yongliang Wang, Xiaobo Li, and Si Liu. GEN-VLKT: Simplify association and enhance interaction understanding for HOI detection. In *CVPR*, 2022. 4, 6, 7, 10
- [37] Tsung-Yi Lin, Michael Maire, Serge J. Belongie, James Hays, Pietro Perona, Deva Ramanan, Piotr Dollár, and C. Lawrence Zitnick. Microsoft COCO: Common objects in context. In *ECCV*, 2014. 3, 5
- [38] Chang Liu, Yinpeng Dong, Wenzhao Xiang, Xiao Yang, Hang Su, Jun Zhu, Yuefeng Chen, Yuan He, Hui Xue, and Shibao Zheng. A comprehensive study on robustness of image classification models: Benchmarking and rethinking. *International Journal of Computer Vision*, 2024. 3
- [39] Hongbin Liu, Moyang Guo, Zhengyuan Jiang, Lun Wang, and Neil Gong. AudioMarkBench: Benchmarking robustness of audio watermarking. In *NeurIPS*, 2024. 3
- [40] Jiawei Liu, Zhijie Wang, Lei Ma, Chunrong Fang, Tongtong Bai, Xufan Zhang, Jia Liu, and Zhenyu Chen. Benchmarking object detection robustness against real-world corruptions. *International Journal of Computer Vision*, 2024. 3
- [41] Ze Liu, Yutong Lin, Yue Cao, Han Hu, Yixuan Wei, Zheng Zhang, Stephen Lin, and Baining Guo. Swin transformer: Hierarchical vision transformer using shifted windows. In *ICCV*, 2021. 5, 6
- [42] Ilya Loshchilov and Frank Hutter. Decoupled weight decay regularization. In *ICLR*, 2019. 6
- [43] Shuailei Ma, Yuefeng Wang, Shanze Wang, and Ying Wei. FGAHOI: Fine-grained anchors for human-object interaction detection. *IEEE Transactions on Pattern Analysis and Machine Intelligence*, 2024. 4, 6
- [44] Sihan Ma, Jing Zhang, Qiong Cao, and Dacheng Tao. PoseBench: Benchmarking the robustness of pose estimation models under corruptions. *arXiv preprint arXiv:2406.14367*, 2024. 3
- [45] Manuel Martin, Alina Roitberg, Monica Haurilet, Matthias Horne, Simon Reiß, Michael Voit, and Rainer Stiefelhagen. Drive&Act: A multi-modal dataset for fine-grained driver behavior recognition in autonomous vehicles. In *ICCV*, 2019. 1
- [46] Claudio Michaelis, Benjamin Mitzkus, Robert Geirhos, Evgenia Rusak, Oliver Bringmann, Alexander S. Ecker, Matthias Bethge, and Wieland Brendel. Benchmarking robustness in object detection: Autonomous driving when winter is coming. *arXiv preprint arXiv:1907.07484*, 2019. 3
- [47] Seonwook Park, Xucong Zhang, Andreas Bulling, and Otmar Hilliges. Learning to find eye region landmarks for remote gaze estimation in unconstrained settings. In *ETRA*, 2018. 2
- [48] Kunyu Peng, Alina Roitberg, Kailun Yang, Jiaming Zhang, and Rainer Stiefelhagen. TransDARC: Transformer-based driver activity recognition with latent space feature calibration. In *IROS*, 2022. 1
- [49] Kunyu Peng, Alina Roitberg, Kailun Yang, Jiaming Zhang, and Rainer Stiefelhagen. Delving deep into one-shot skeleton-based action recognition with diverse occlusions. *IEEE Transactions on Pattern Analysis and Machine Intelligence*, 2023. 3
- [50] Alessandro Prest, Vittorio Ferrari, and Cordelia Schmid. Explicit modeling of human-object interactions in realistic videos. *IEEE Transactions on Pattern Analysis and Machine Intelligence*, 2013. 1
- [51] Siyuan Qi, Wenguan Wang, Baoxiong Jia, Jianbing Shen, and Song-Chun Zhu. Learning human-object interactions by graph parsing neural networks. In *ECCV*, 2018. 2
- [52] Shaoqing Ren, Kaiming He, Ross Girshick, and Jian Sun. Faster R-CNN: Towards real-time object detection with region proposal networks. In *NeurIPS*, 2015. 2
- [53] Soumyendu Sarkar, Ashwin Ramesh Babu, Sajad Mousavi, Zachariah Carmichael, Vineet Gundecha, Sahand Ghorbanpour, Ricardo Luna Gutierrez, Antonio Guillen, and Avisek Naug. Benchmark generation framework with customizable distortions for image classifier robustness. In *WACV*, 2024. 3
- [54] Madeline Chantry Schiappa, Shehreen Azad, Sachidanand VS, Yunhao Ge, Ondrej Miksik, Yogesh S. Rawat, and Vibhav Vineet. Robustness analysis on foundational segmentation models. In *CVPR*, 2024. 3
- [55] Shuai Shao, Zeming Li, Tianyuan Zhang, Chao Peng, Gang Yu, Xiangyu Zhang, Jing Li, and Jian Sun. Objects365: A large-scale, high-quality dataset for object detection. In *ICCV*, 2019. 5
- [56] Masato Tamura, Hiroki Ohashi, and Tomoaki Yoshinaga. QPIC: Query-based pairwise human-object interaction detection with image-wide contextual information. In *CVPR*, 2021. 1, 3, 6
- [57] Danyang Tu, Wei Sun, Guangtao Zhai, and Wei Shen. Agglomerative transformer for human-object interaction detection. In *CVPR*, 2023. 1
- [58] Oytun Ulutan, A. S. M. Iftekhar, and Bangalore S. Manjunath. VSGNet: Spatial attention network for detecting human object interactions using graph convolutions. In *CVPR*, 2020. 2
- [59] Bo Wan, Desen Zhou, Yongfei Liu, Rongjie Li, and Xuming He. Pose-aware multi-level feature network for human object interaction detection. In *ICCV*, 2019. 2
- [60] Chen Wang, Angtian Wang, Junbo Li, Alan Yuille, and Cihang Xie. Benchmarking robustness in neural radiance fields. In *CVPR*, 2024. 3
- [61] Haoran Wang, Licheng Jiao, Fang Liu, Lingling Li, Xu Liu, Deyi Ji, and Weihao Gan. IPGN: Interactiveness proposal graph network for human-object interaction detection. *TIP*, 2021. 2

- [62] Tiancai Wang, Tong Yang, Martin Danelljan, Fahad Shahbaz Khan, Xiangyu Zhang, and Jian Sun. Learning human-object interaction detection using interaction points. In *CVPR*, 2020. 3, 4, 6, 8
- [63] Shaoyuan Xie, Lingdong Kong, Wenwei Zhang, Jiawei Ren, Liang Pan, Kai Chen, and Ziwei Liu. Benchmarking and improving bird’s eye view perception robustness in autonomous driving. *IEEE Transactions on Pattern Analysis and Machine Intelligence*, 2025. 3
- [64] Bingjie Xu, Yongkang Wong, Junnan Li, Qi Zhao, and Mohan S. Kankanhalli. Learning to detect human-object interactions with knowledge. In *CVPR*, 2019. 2, 9
- [65] Bingjie Xu, Junnan Li, Yongkang Wong, Qi Zhao, and Mohan S. Kankanhalli. Interact as you intend: Intention-driven human-object interaction detection. *IEEE Transactions on Multimedia*, 2020. 1, 2
- [66] Jie Yang, Bingliang Li, Fengyu Yang, Ailing Zeng, Lei Zhang, and Ruimao Zhang. Boosting human-object interaction detection with text-to-image diffusion model. *arXiv preprint arXiv:2305.12252*, 2023. 3, 6
- [67] Bangpeng Yao and Li Fei-Fei. Modeling mutual context of object and human pose in human-object interaction activities. In *CVPR*, 2010. 2
- [68] Zhonghua Yi, Hao Shi, Qi Jiang, Yao Gao, Ze Wang, Yufan Zhang, Kailun Yang, and Kaiwei Wang. Benchmarking the robustness of optical flow estimation to corruptions. *arXiv preprint arXiv:2411.14865*, 2024. 3
- [69] Yu Yu, Gang Liu, and Jean-Marc Odobez. Deep multitask gaze estimation with a constrained landmark-gaze model. In *ECCVW*, 2018. 2
- [70] Hangjie Yuan, Shiwei Zhang, Xiang Wang, Samuel Albanie, Yining Pan, Tao Feng, Jianwen Jiang, Dong Ni, Yingya Zhang, and Deli Zhao. RLIPv2: Fast scaling of relational language-image pre-training. In *ICCV*, 2023. 2, 4, 5, 6, 8, 10
- [71] Runhao Zeng, Xiaoyong Chen, Jiaming Liang, Huisi Wu, Guangzhong Cao, and Yong Guo. Benchmarking the robustness of temporal action detection models against temporal corruptions. In *CVPR*, 2024. 3
- [72] Aixi Zhang, Yue Liao, Si Liu, Miao Lu, Yongliang Wang, Chen Gao, and Xiaobo Li. Mining the benefits of two-stage and one-stage hoi detection. In *NeurIPS*, 2021. 3, 6, 7, 10
- [73] Frederic Z Zhang, Dylan Campbell, and Stephen Gould. Spatially conditioned graphs for detecting human-object interactions. In *ICCV*, 2021. 2
- [74] Frederic Z. Zhang, Dylan Campbell, and Stephen Gould. Efficient two-stage detection of human-object interactions with a novel unary-pairwise transformer. In *CVPR*, 2022. 2, 3, 6, 7
- [75] Frederic Z. Zhang, Yuhui Yuan, Dylan Campbell, Zhuoyao Zhong, and Stephen Gould. Exploring predicate visual context in detecting of human-object interactions. In *ICCV*, 2023. 2
- [76] Tienong Zhang, Yuqing Cui, and Wei Fang. Integrative human and object aware online progress observation for human-centric augmented reality assembly. *Advanced Engineering Informatics*, 2025. 1
- [77] Xucong Zhang, Yusuke Sugano, Mario Fritz, and Andreas Bulling. Appearance-based gaze estimation in the wild. In *CVPR*, 2015. 2
- [78] Yong Zhang, Yingwei Pan, Ting Yao, Rui Huang, Tao Mei, and Chang-Wen Chen. Exploring structure-aware transformer over interaction proposals for human-object interaction detection. In *CVPR*, 2022. 1
- [79] Xubin Zhong, Xian Qu, Changxing Ding, and Dacheng Tao. Glance and gaze: Inferring action-aware points for one-stage human-object interaction detection. In *CVPR*, 2021. 2
- [80] Penghao Zhou and Mingmin Chi. Relation parsing neural network for human-object interaction detection. In *ICCV*, 2019. 2
- [81] Tianfei Zhou, Wenguan Wang, Siyuan Qi, Haibin Ling, and Jianbing Shen. Cascaded human-object interaction recognition. In *CVPR*, 2020. 2
- [82] Cheng Zou, Bohan Wang, Yue Hu, Junqi Liu, Qian Wu, Yu Zhao, Boxun Li, Chenguang Zhang, Chi Zhang, Yichen Wei, and Jian Sun. End-to-end human object interaction detection with hoi transformer. In *CVPR*, 2021. 1